

*School of Natural Sciences and Mathematics*

***One-Dimensional Full Wave Simulation of  
Equatorial Magnetosonic Wave Propagation  
in an Inhomogeneous Magnetosphere***

**UT Dallas Author(s):**

Xu Liu  
Lunjin Chen  
Lixia Yang  
Zhiyang Xia

**Rights:**

©2018 American Geophysical Union. All Rights Reserved.

**Citation:**

Liu, Xu, Lunjin Chen, Lixia Yang, Zhiyang Xia, et al. 2018. "One-dimensional full wave simulation of equatorial magnetosonic wave propagation in an inhomogeneous magnetosphere." *Journal of Geophysical Research-Space Physics* 123: 587-599, doi:10.1002/2017JA024336

*This document is being made freely available by the Eugene McDermott Library of the University of Texas at Dallas with permission of the copyright owner. All rights are reserved under United States copyright law unless specified otherwise.*

## RESEARCH ARTICLE

10.1002/2017JA024336

## Key Points:

- Without plasmopause, radially propagating MS waves can propagate down to the ionospheric height if no damping mechanism is considered
- A small portion of the MS wave power is reflected by a typical plasmopause, where WKB approximation is generally valid
- Multiple fine-scale density irregularities near the outer edge of plasmopause can effectively block the MS wave propagation

## Correspondence to:

X. Liu,  
xu.liu1@utdallas.edu

## Citation:

Liu, X., Chen, L., Yang, L., Xia, Z., & Malaspina, D. M. (2018). One-dimensional full wave simulation of equatorial magnetosonic wave propagation in an inhomogeneous magnetosphere. *Journal of Geophysical Research: Space Physics*, 123, 587–599. <https://doi.org/10.1002/2017JA024336>

Received 7 MAY 2017

Accepted 22 DEC 2017

Accepted article online 3 JAN 2018

Published online 30 JAN 2018

## One-Dimensional Full Wave Simulation of Equatorial Magnetosonic Wave Propagation in an Inhomogeneous Magnetosphere

Xu Liu<sup>1</sup> , Lunjin Chen<sup>1</sup> , Lixia Yang<sup>1,2</sup>, Zhiyang Xia<sup>1</sup> , and David M. Malaspina<sup>3</sup> 

<sup>1</sup>William B. Hanson Center for Space Sciences, University of Texas at Dallas, Richardson, TX, USA, <sup>2</sup>Department of Communication Engineering, Jiangsu University, Jiangsu, China, <sup>3</sup>Laboratory for Atmospheric and Space Physics, University of Colorado Boulder, Boulder, CO, USA

**Abstract** The effect of the plasmopause on equatorially radially propagating fast magnetosonic (MS) waves in the Earth's dipole magnetic field is studied by using finite difference time domain method. We run 1-D simulation for three different density profiles: (1) no plasmopause, (2) with a plasmopause, and (3) with a plasmopause accompanied with fine-scale density irregularity. We find that (1) without plasmopause the radially inward propagating MS wave can reach ionosphere and continuously propagate to lower altitude if no damping mechanism is considered. The wave properties follow the cold plasma dispersion relation locally along its trajectory. (2) For simulation with a plasmopause with a scale length of  $0.006 R_E$  compared to wavelength, only a small fraction of the MS wave power is reflected by the plasmopause. WKB approximation is generally valid for such plasmopause. (3) The multiple fine-scale density irregularities near the outer edge of plasmopause can effectively block the MS wave propagation, resulting in a terminating boundary for MS waves near the plasmopause.

### 1. Introduction

Fast magnetosonic (MS) waves are the low-frequency extension of electromagnetic emission between the proton gyrofrequency and the lower hybrid resonant frequency in the whistler mode branch (Fu et al., 2014; Laakso et al., 1990; Perraut et al., 1982; Santolík et al., 2004). The wave magnetic field is nearly linearly polarized along the background magnetic field, while wave electric fields are mostly in the plane perpendicular to the background magnetic field. These emissions are also known as equatorial noise, equatorial MS waves, and ion Bernstein modes. The observation reveals that the emissions can appear as discrete frequency spectra with frequency spacing equal to proton gyrofrequency (e.g., Balikhin et al., 2015). The generation of discrete and continuous frequency spectra has been investigated thoroughly by (Sun, Gao, Chen, et al., 2016; Sun, Gao, Lu, 2016). They are confined within  $\pm 10^\circ$  of geomagnetic equator (Gurnett, 1976; Němec et al., 2005; Olsen et al., 1987; Russell et al., 1970; Santolík et al., 2002). Zhima et al. (2015) reported observations of magnetosonic wave well off the equator at geomagnetic latitudes from  $16.5^\circ$  to  $17.9^\circ$  and  $L$  shells from  $\sim 2.7$  to 4.6. A recent statistical study of these waves (Boardsen et al., 2016) finds a frequency-dependent latitudinal distribution with a tail that extends up to  $\sim 20^\circ$ .

Ray tracing results (e.g., Chen & Thorne, 2012; Xiao et al., 2012) demonstrate that equatorial MS waves can propagate radially and azimuthally. MS waves in a narrow radial region near the plasmopause can migrate globally over local times. MS waves at high  $L$  shells (outside the plasmopause) are confined in a relatively narrow MLT interval. Cluster observations (Hrbáčková et al., 2015) show consistent results where the MS waves inside the plasmopause are found all over the MLT while the MS waves outside the plasmopause are observed relatively narrow from 10 to 18 h MLT.

The ray tracing result also shows that the radially propagating MS waves can propagate across the plasmopause and all the way to a very low altitude on the equatorial plane, which is confirmed by observations. On the one hand, wave propagation across the plasmopause, as shown in Figure 2 of Boardsen et al. (2014), can take place when the density gradient is small. On the other hand, one rare event report by Santolík et al. (2016) shows that a MS emission can access down to low altitude ( $\sim 700$  km) near the equatorial plane

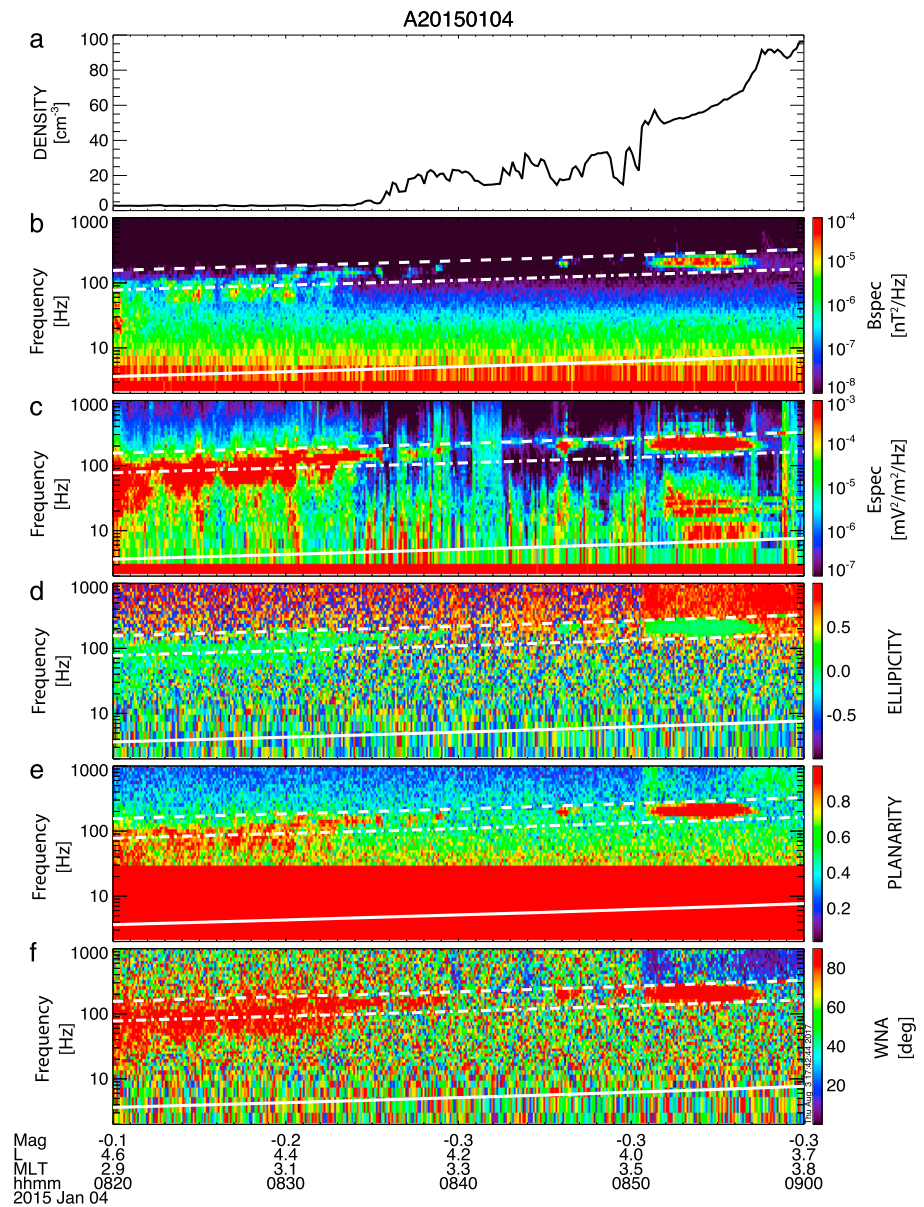


**Figure 1.** Van Allen Probes observation of MS wave terminated by plasmopause. (a) Plasma density. (b) Total magnetic power spectrum. (c) Total electric power spectrum in the spacecraft spin plane. (d) Ellipticity. (e) Planarity. (f) Wave normal angle. Two white dashed lines in each panel from top to bottom are lower hybrid frequency and half lower hybrid frequency. The solid line denotes proton gyrofrequency.

from DEMETER observation. The observed MS emission, whose frequency is less than the local proton gyrofrequency, is an indication of earthward propagation from higher *L* shell to this altitude.

Although there is consistency between simulation and observation studies above, observationally, the plasmopause often serves a nice boundary for MS wave emission. Figure 1 shows MS wave observation by Van Allen Radiation Belt Storm Probes A (RBSP A) (Mauk et al., 2013) on 4 January 2015. The plasma density (Figure 1a) is derived from the spacecraft potential observed by the Electric Field and Waves Suite (EFW) (Wygant et al., 2013). The wave magnetic power spectrum (Figure 1b) and electric power spectrum (Figure 1c) are observed by the Electric and Magnetic Field Instrument and Integrated Science (EMFISIS) waves instrument (Kletzing et al., 2013). Figures 1d–1f show ellipticity, planarity, and wave normal angle, respectively. When the inbound spacecraft passed through the plasmopause, two distinct MS wave events (below the lower hybrid resonant frequency) can be identified: one confined outside the plasmopause observed from

08:20 UT to 08:40 UT and the other confined inside the plasmopause observed from 08:51 UT to 08:57 UT. The differences in wave power and frequency ranges indicate that the two MS waves are separate emissions. They are well separated by the plasmopause boundary layer, whose outer edge is accompanied by fine-scale density irregularities.

The discrepancy between ray tracing prediction (i.e., allowing wave propagation through the plasmopause) and the RBSP observations above near the plasmopause region indicates that full wave solution is required for MS waves. Ray tracing method in the frame of geometrical optics is based on WKB assumption ( $\sim e^{i(\mathbf{k}(\mathbf{r})\cdot\mathbf{r}-i\nu t)}$ ); that is, the wavelength should be sufficiently small compared with spatial scale of background medium variation. Under this assumption wave reflection that corresponds to wave number  $k = 0$  is impossible. The WKB approximation for lower frequency (with larger wavelength) of MS waves may be invalid in certain regions, for instance, near the plasmopause region, where fine-scale density irregularities are often found.

In this study, we study perpendicular propagation of MS waves. Although resonant instability of MS waves due to proton ring distribution requires a finite parallel wave number, nonresonant instability can take place at exactly perpendicular propagation (Gul'elmi et al., 1975), whose growth rate can exceed those at less oblique angles (Figure 1 of Chen, 2015). Observationally, it is difficult to resolve wave normal angle near  $90^\circ$  within accuracy of several degrees using magnetic field vector perturbation. Previous ray tracing results (Chen & Thorne, 2012) show similar trajectories projected on the equatorial plane of MS waves with nearly perpendicular propagation wave normal angle to that for exactly perpendicular propagation. For our purpose of examining the wave propagation, we merely focus on the exactly perpendicular propagation in the radial direction, to gain insights for MS wave propagation. We use finite difference time domain (FDTD) method to obtain full wave solution for radially propagating MS waves and examine the effect of plasmopause and the fine-scale density structure on the wave propagation. Here is the organization of the paper. The method description is given in section 2. Section 3 shows simulation results followed by discussion and conclusion in section 4.

## 2. FDTD Method

FDTD is a numerical algorithm used for modeling computational electrodynamics in the time domain. It can be used to solve fully electromagnetic wave equations. The equations for three-dimensional wave propagation in a plasma of two cold species (protons and electrons) are

$$\nabla \times \mathbf{E} = -\mu_0 \frac{\partial \mathbf{H}}{\partial t} \quad (1)$$

$$\nabla \times \mathbf{H} = \epsilon_0 \frac{\partial \mathbf{E}}{\partial t} + \sum_{\alpha} \mathbf{J}_{\alpha} \quad (2)$$

$$\frac{\partial \mathbf{J}_{\alpha}}{\partial t} + \nu_{\alpha} \mathbf{J}_{\alpha} = \epsilon_0 \omega_{p\alpha}^2 \mathbf{E} - \mathbf{\Omega}_{\alpha} \times \mathbf{J}_{\alpha} \quad (3)$$

where  $\alpha$  denotes species (protons and electrons),  $\nu_{\alpha}$  is collisional frequency for  $\alpha$  species,  $\omega_{p\alpha}$  is plasma frequency for  $\alpha$  species, and  $\mathbf{\Omega}_{\alpha}$  is gyrofrequency for  $\alpha$  species.  $\mathbf{E}$  and  $\mathbf{H}$  are electric field and magnetic field, respectively.  $\mathbf{J}_{\alpha}$  is electric current carried by  $\alpha$  species.  $\mu_0$  and  $\epsilon_0$  are permeability and permittivity in vacuum, respectively. The first two equations are Maxwell's equations. The third equation for the current is based on the linearized momentum equation of cold species  $\alpha$ .

Considering the MS wave radial propagation toward Earth in the equatorial plane, we adopt equations for MS wave propagation in one dimension (radial dimension)

$$\frac{\partial E_y}{\partial x} = -\mu_0 \frac{\partial H_z}{\partial t} \quad (4)$$

$$-\frac{\partial H_z}{\partial x} = \epsilon_0 \frac{\partial E_y}{\partial t} + \sum_{\alpha} J_{y\alpha} \quad (5)$$

$$0 = \epsilon_0 \frac{\partial E_x}{\partial t} + \sum_{\alpha} J_{x\alpha} \quad (6)$$

$$\frac{\partial J_{x\alpha}}{\partial t} + \nu_{\alpha} J_{x\alpha} = \epsilon_0 \omega_{p\alpha}^2 E_x + \mathbf{\Omega}_{\alpha} J_{y\alpha} \quad (7)$$

$$\frac{\partial J_{y\alpha}}{\partial t} + \nu_{\alpha} J_{y\alpha} = \epsilon_0 \omega_{p\alpha}^2 E_y - \mathbf{\Omega}_{\alpha} J_{x\alpha} \quad (8)$$

$v_\alpha$  is set to be an artificially large number in the absorbing boundary layer (at the two sides of the simulation region, where the waves are damped quickly in order to avoid unphysical reflection into the simulation region due to the boundary) and  $v_\alpha = 0$  inside the simulation region (nearly collisionless nature of magnetospheric plasma).  $Z$  axis is along background magnetic field direction.  $X$  axis is radial direction, and  $Y$  axis is determined by completing the right-hand coordinate system. The numerical calculation procedures follow Yang et al. (2011) and are summarized briefly here. The time and spatial grids for each quantity are  $H_z(m + \frac{1}{2}, j + \frac{1}{2})$ ,  $E_x(m, j + \frac{1}{2})$ ,  $E_y(m, j)$ ,  $J_x(m + \frac{1}{2}, j + \frac{1}{2})$ , and  $J_y(m + \frac{1}{2}, j + \frac{1}{2})$ , in which  $m$  and  $j$  represent integer grid of time and position, respectively.

Initial values of  $H_z$ ,  $J_x$ , and  $J_y$  at time  $t = \frac{1}{2}$  and initial values of  $E_x$  and  $E_y$  at time  $t = 0$  for any given position in simulation domain are set to zero. Values of  $H_z$  component at time  $m + \frac{1}{2}$  are updated by values of  $E_y$  component at time  $m$  and  $H_z$  component at time  $m - \frac{1}{2}$  via equation (4). Values of  $J_{x\alpha}$  and  $J_{y\alpha}$  components at time  $m + \frac{1}{2}$  are updated by values of  $E_x$  and  $E_y$  at times  $m$  and  $J_{x\alpha}$  and  $J_{y\alpha}$  at time  $m - \frac{1}{2}$  via equations (7) and (8). Values of  $E_x$  and  $E_y$  components at time  $m + 1$  are updated by values of  $E_x$  and  $E_y$  at times  $m$  and  $J_{x\alpha}$  and  $J_{y\alpha}$  and  $H_z$  components at time  $m + \frac{1}{2}$  via equations (5) and (6). After the quantities at all grids in the space domain are updated, the iteration advances to next time step.

It is worthy mentioning that the Laplace transform and inverse Laplace transform are used to evaluate equations (7) and (8) to minimize the numerical error, following the algorithm proposed by Yang et al. (2011) and Xie and Yang (2011). We use absorbing boundary conditions (large  $v_\alpha$ ) for both the inner and outer boundaries (Shi et al., 2015). The wave power is quickly attenuated in the boundary layers by taking advantage of the damping term containing  $v_\alpha$  in equation (3), to ensure little reflection back to the simulation region. For this type of boundary conditions, the choices of inner and outer boundary locations are not critical for simulation, as long as the MS waves are sufficiently absorbed outside the region of interest.

We set up a sine function with a fixed frequency  $f$  for  $B_z$  component at a fixed source location as a soft source. The  $B_z$  component at source location is mandatorily updated by the summation of prescribed sinusoidal oscillation and the result updated by the FDTD algorithm. By doing so, we can eliminate artificial reflection at the source location, which can occur for a hard source. The other field components at the source location and all wave field components at other locations are updated self-consistently by the FDTD method.

### 3. Simulation Results

We will simulate wave propagation in a magnetospheric medium. A dipole magnetic field is used to represent Earth's magnetic field throughout the paper. We vary the background plasma density profile to examine the effect of plasma density distribution on MS wave propagation.

#### 3.1. MS Wave Propagation Without Plasmopause

First, we examine the MS wave for slowly varying plasma density without plasmopause. We set up the plasma density as below:

$$n = 100 \text{ cm}^{-3} \text{ for } L \leq 3.1$$

$$n = 1 + 99 \exp \left[ - \left( \frac{L - 3.1}{\beta} \right)^2 \right] \text{ cm}^{-3} \text{ for } L > 3.1 \quad (9)$$

The density is a constant of  $100 \text{ cm}^{-3}$  at  $L < 3.1$  and then decreases exponentially toward a constant of  $1 \text{ cm}^{-3}$  as  $L$  increases above 3.1.  $\beta$  is set to 0.7306 so that the density profile varies smoothly in the simulation region between  $L = 2.5$  and  $L = 5.02$ .

Figure 2a shows the spatial profile of the plasma density in the blue line and background dipole magnetic field strength in the red line. For convenience, we use  $(\frac{\omega}{\Omega_{cp}})_s$  to represent the ratio of wave frequency to the proton gyrofrequency at the source location  $L_{\text{source}} = 5$ . The wave frequency is set as  $(\frac{\omega}{\Omega_{cp}})_s = 5$ . Figures 2b–2e show simulated fields  $E_x$ ,  $E_y$ ,  $cB_z$ , and  $J_y$  as a function of location  $L$  and time  $t$ , where  $c$  is the light speed in vacuum and  $B_z = \mu_0 H_z$ . Figures 2f and 2g show the electromagnetic energy density  $W_{\text{em}} (= \frac{1}{2\mu_0} B_z^2 + \frac{1}{2\epsilon_0} (E_x^2 + E_y^2))$  and total kinetic energy density  $W_k (= \sum_{\alpha} \frac{1}{2} n m_{\alpha} (v_{\alpha x}^2 + v_{\alpha y}^2))$ . As the wave propagates inward, the normalized wave frequency  $\frac{\omega}{\Omega_{cp}}$  decreases and the wave can pass through  $\frac{\omega}{\Omega_{cp}} = 1$  when  $L \sim 2.9$  (dashed line). After check, the simulated wave properties ( $E_x$ ,  $E_y$ ,  $cB_z$ ,  $J_y$ ,  $W_k$ , and  $W_{\text{em}}$ ) are consistent with the local cold plasma dispersion

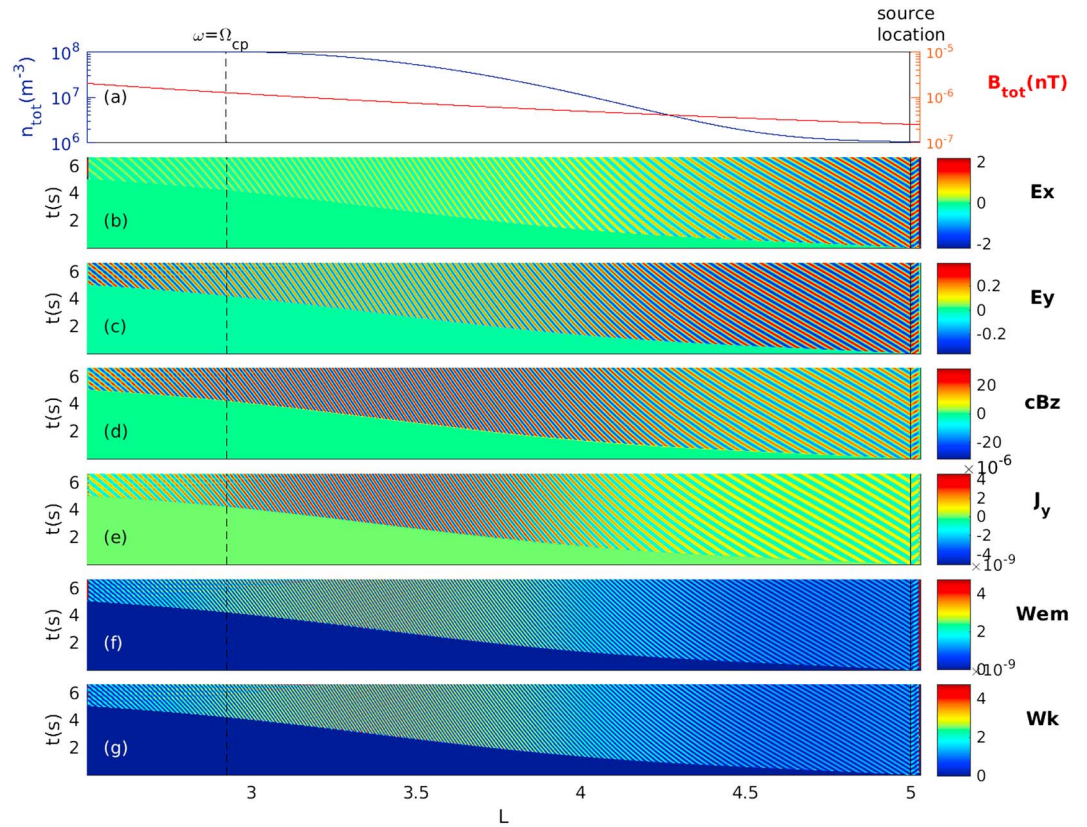


**Figure 2.** MS wave propagation simulation without plasmopause. Vertical axis is simulation time. (a) Plasma density (blue) and background magnetic field (red line). (b)  $E_x$ , (c)  $E_y$ , (d) light speed  $c$  in vacuum times  $B_z$ , and (e) plasma current in  $y$  direction. (f) Electromagnetic energy density and (g) plasma kinetic energy density. The source frequency  $(\frac{\omega}{\Omega_{cp}})_s = 5$ . The source location at  $5 R_E$  is marked by a black solid line, and wave frequency is equal to local proton gyrofrequency at  $2.9 R_E$ , marked by a black dashed line.

relation. The gradually varying density profile does not prevent the MS wave energy from transporting to lower  $L$  shell region and even to the ionosphere (not shown).

Now we examine the effect of the ionosphere on the wave propagation, shown in Figure 3. We set up the plasma density using the modified diffusive equilibrium model (Bortnik et al., 2011) (Figure 3a). The wave source is set with the same absolute wave frequency as Figure 2 ( $(\frac{\omega}{\Omega_{cp}})_s = 5$  at  $L = 5$ ) and locates at  $L_{source} = 1.4$ . The dramatically varying plasma density associated with the ionosphere results in weak wave reflections at  $L = 1.03$  and  $L = 1.175$  (two black dashed lines in Figure 3), respectively. Two weak standing waves form from  $L = 1.03$  to  $L = 1.15$  and from  $L = 1.175$  to  $L = 1.4$ , respectively. In our simulation, we only consider proton and electron species. But in the ionosphere, the presence of heavier ions, which leads to a smaller Alfvénic speed and thus a smaller wavelength for a fixed frequency, may result in a weaker wave reflection than that in Figure 3. The MS wave propagation simulations with slowly varying plasma density in the inner magnetosphere and diffusive equilibrium plasma density in the ionosphere show that the MS wave generated in the magnetosphere can radially propagate down to the ionosphere, which indicates that the MS wave damping must play an important role to determine whether the MS wave can be observed in the ionosphere.

### 3.2. MS Wave Propagation With a Plasmopause

Now we consider MS wave propagation properties in the Earth’s dipole magnetic field with a plasmopause. The density profile adopts

$$n = \frac{n_{in} + n_{out}}{2} - \frac{n_{in} - n_{out}}{2} \tanh \left( 4.56 \frac{L - L_{pp}}{\Delta L_{pp}} \right) \quad (10)$$

where  $n_{in} = 100 \text{ cm}^{-3}$  and  $n_{out} = 1 \text{ cm}^{-3}$  are the plasma density inside and outside the plasmopause, respectively. A factor of 4.56 in equation (10) is used to ensure that the plasma density increases from  $2 \text{ cm}^{-3}$

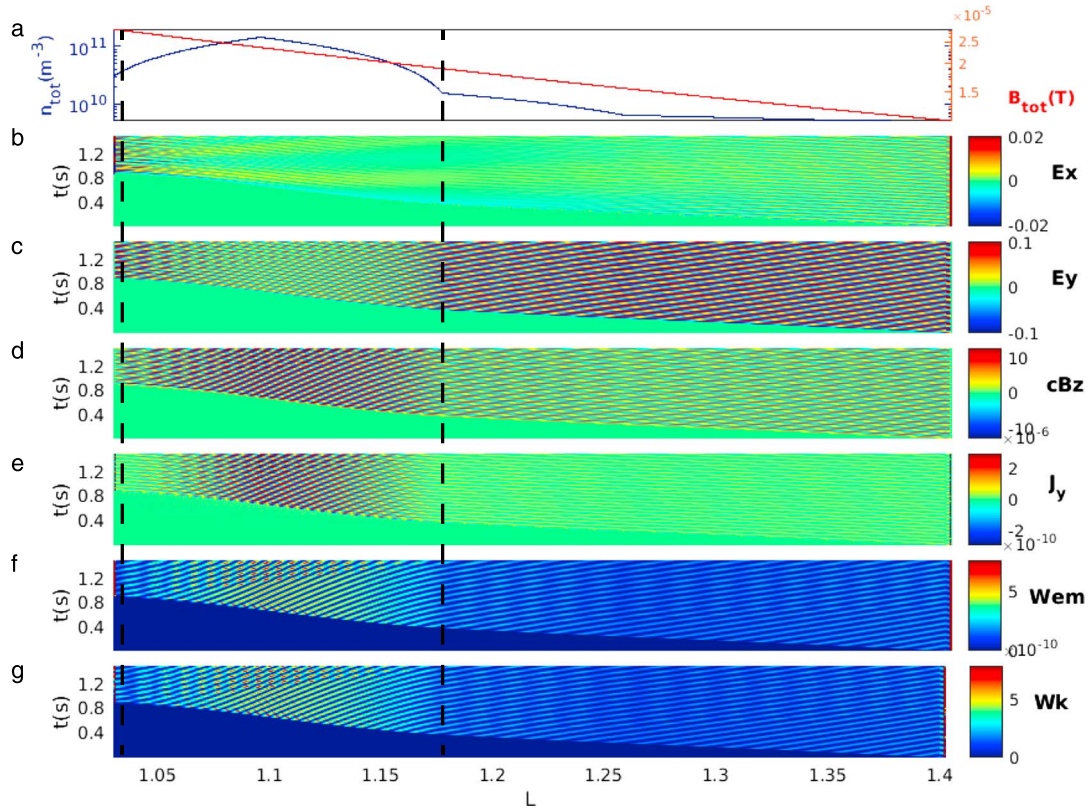


**Figure 3.** MS wave propagation simulation with ionosphere in similar format to Figure 2. Source location is at  $L_{\text{source}} = 1.4$ . The source frequency is the same as Figure 2 ( $(\frac{\omega}{\Omega_{cp}})_s = 5$  at  $L = 5$ ). Wave reflection locations are marked by two black dashed lines.

to  $99 \text{ cm}^{-3}$  over a spatial range of  $\Delta L_{\text{pp}}$ , which is defined as the plasmopause width. The plasmopause center location  $L_{\text{pp}}$  and the plasmopause width  $\Delta L_{\text{pp}}$  are set to 4.94 and 0.03, respectively.

Figure 4a shows the spatial profile of the plasma density by the blue line and background dipole magnetic field strength by the red line. Figures 4b–4d show the simulated  $E_x$ ,  $E_y$ , and  $cB_z$  as a function of location  $L$  and time  $t$ . The source location and frequency of MS wave are the same as Figure 2. The spatially varying medium near the plasmopause region leads to partial reflection and partial transmission across the plasmopause. Quantification of reflection and transmission coefficients due to the plasmopause is done by the following three steps.

1. We treat plasmopause region as a box with inner edge at  $L_1$  and outer edge at  $L_2$  (as shown in Figure 4a). The incident wave enters the box. The reflected wave leaves the box to the right, and transmitted wave leaves the box to the left. We approximate transmitted waves on the lower  $L$  side of the box as a plane wave propagating to the left and approximate the waves on the higher  $L$  side of the box as a sum of two plane waves propagating in the opposite direction. The approximation is reasonable because density varies slowly with  $L$  outside the box.
2. We decompose the simulated fields at  $L_2$  into components of two plane waves with opposite propagation directions. According to the cold plasma dispersion relation, the fields of the two plane waves satisfy

$$\tilde{E}_{y\pm} = \frac{S}{iD} \tilde{E}_{x\pm} \tag{11}$$

$$c\tilde{B}_{z\pm} = \frac{\pm\eta S}{iD} \tilde{E}_{x\pm} \tag{12}$$

where  $\eta$  is wave refraction index and  $S$  and  $D$  are Stix notations (Stix, 1992).  $\tilde{E}_{x\pm}$ ,  $\tilde{E}_{y\pm}$ , and  $\tilde{B}_{z\pm}$  are complex wave amplitudes. Plus and minus signs denote outward and inward propagation directions, respectively. At the given location  $L_2$  we analyze the time series of simulated  $E_x$  and  $B_z$  components by fast Fourier transform to get the total complex amplitudes for  $x$  component of electric field  $\tilde{E}_x$  and for  $z$  component of magnetic

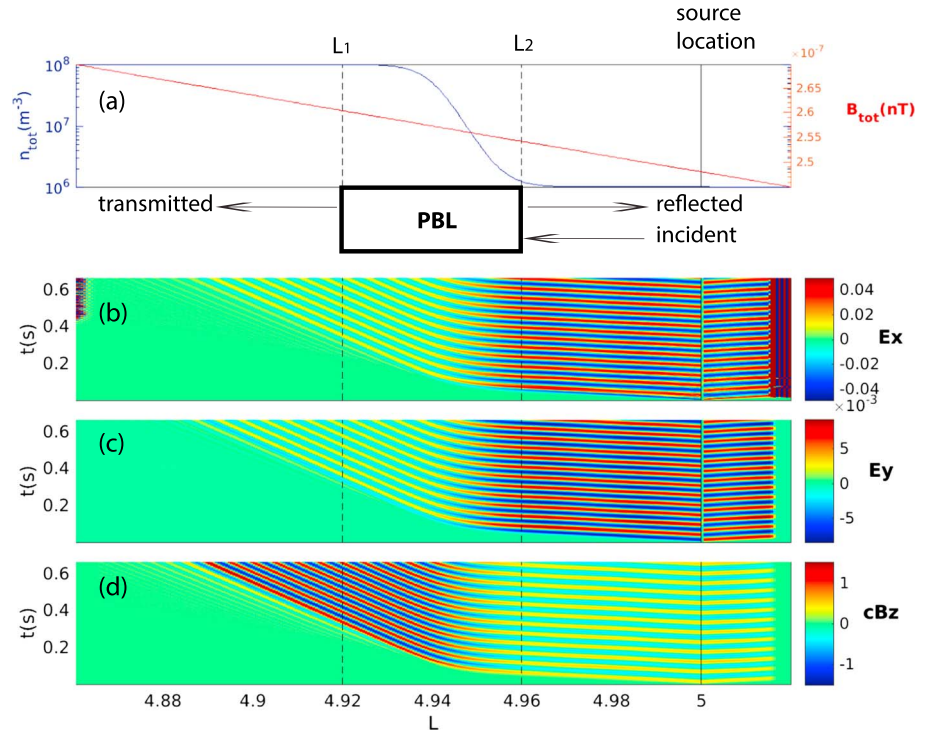


**Figure 4.** MS wave propagation simulation with a plasmopause. (a) Plasma density (blue) and background magnetic field (red line), (b)  $E_x$ , (c)  $E_y$ , and (d) light speed  $c$  in vacuum times  $B_z$ . The source frequency  $(\frac{\omega}{\Omega_{cp}})_s = 5$ . The source location (at  $5 R_E$ ) is marked by the black solid line, and plasmopause center location is set at  $4.93 R_E$ . Between the two dashed lines is the plasmopause boundary layer (PBL), illustrated by the rectangular box. Incident wave propagates into the PBL region, while reflected wave is reflected by PBL region and transmitted wave is leaving PBL region.

field  $\tilde{B}_z$  when the system reaches a quasi steady state. Then we can use total complex wave amplitudes and equations (11) and (12) to separate the complex wave amplitudes of the two plane waves, the incident wave of inward propagation, and the reflected wave of outward propagation. It yields

$$\tilde{E}_{xi} = \frac{1}{2} \left( \tilde{E}_x - \frac{iD}{\eta S} c \tilde{B}_z \right) \quad (13)$$

$$\tilde{E}_{xr} = \frac{1}{2} \left( \tilde{E}_x + \frac{iD}{\eta S} c \tilde{B}_z \right) \quad (14)$$

where the subscripts  $i$  and  $r$  denote the incident and reflected waves, respectively. When applying the same analysis to  $L_1$ , we obtain the complex wave amplitude of the transmitted wave and another small amplitude wave propagating outward. This small amplitude wave is caused by the varying magnetic field, which is negligible compared with the amplitudes of the transmitted wave and the incident wave.

3. For quantifying the effect of the plasmopause on the radial MS wave propagation, we define the wave energy transmission efficiency (WETE) as

$$\text{WETE} = \frac{(\tilde{\mathbf{E}}_t \times \tilde{\mathbf{B}}_t^*)_x}{(\tilde{\mathbf{E}}_i \times \tilde{\mathbf{B}}_i^*)_x} \quad (15)$$

where the subscript  $t$  represents transmitted waves and asterisk represents complex conjugate. Physical meaning of WETE is the ratio of transmitted Poynting flux to incident Poynting flux in  $x$  direction. We use WETE to quantify the effect of the plasmopause on wave propagation. For the case of  $\text{WETE} = 0$ , no wave energy can pass through plasmopause; that is, the wave is totally reflected by the sharp plasmopause. For the case of  $\text{WETE} = 1$ , the wave can propagate through plasmopause without wave power attenuation.

The WETE value evaluated for the above simulation (shown in Figure 4) is 0.875. The outward propagating reflected wave meets the incident wave, leading to a weak standing wave from  $4.94 R_E$  to  $5 R_E$  after

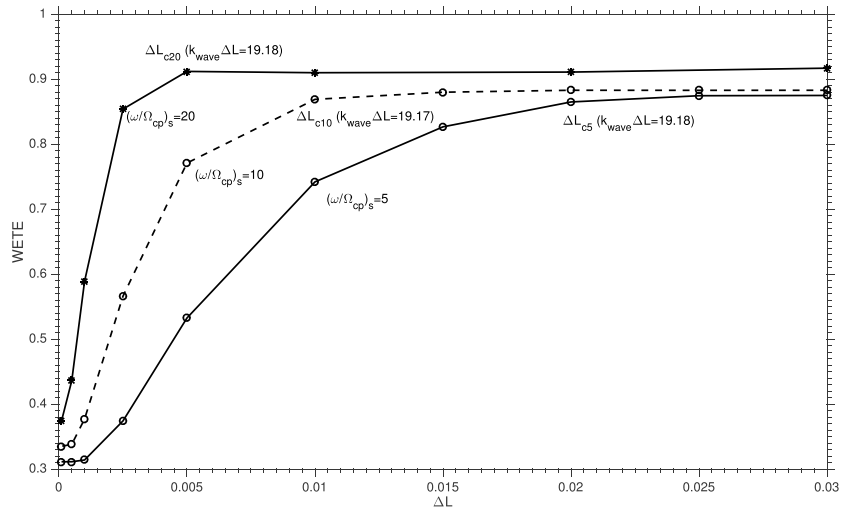


**Figure 5.** WETE versus plasmopause width for the three different frequencies:  $(\frac{\omega}{\Omega_{cp}})_s = 5$  (solid line, circle symbol),  $(\frac{\omega}{\Omega_{cp}})_s = 10$  (dashed line, circle symbol), and  $(\frac{\omega}{\Omega_{cp}})_s = 20$  (solid line, asteroid symbol). Critical values of  $\Delta L_c$  and product of  $k_{wave}\Delta L_c$  are also marked.

0.15 s (Figure 4). The reflected wave power is very weak compared to the incident wave power. For this case where the reflected wave is negligible, the Poynting flux along x axis, which is proportional to  $\eta|\tilde{E}_y|^2$ , is approximately constant in this case. The refraction index of MS waves  $\eta (= RL/S)$ , where R and L are Stix notations, increases with plasma density, so its value inside the plasmasphere is much larger than that outside the plasmasphere. There are several worth noting points regarding variation of electromagnetic fields across the plasmopause. (1)  $|\tilde{E}_y|$  component of incident wave is larger than  $|\tilde{E}_y|$  component of transmitted wave (Figure 4c) because  $\eta\tilde{E}_y^2$  is relatively constant and thus  $\tilde{E}_y \sim \eta^{-1/2}$ . (2) The variation of  $|\tilde{E}_x|$  is similar

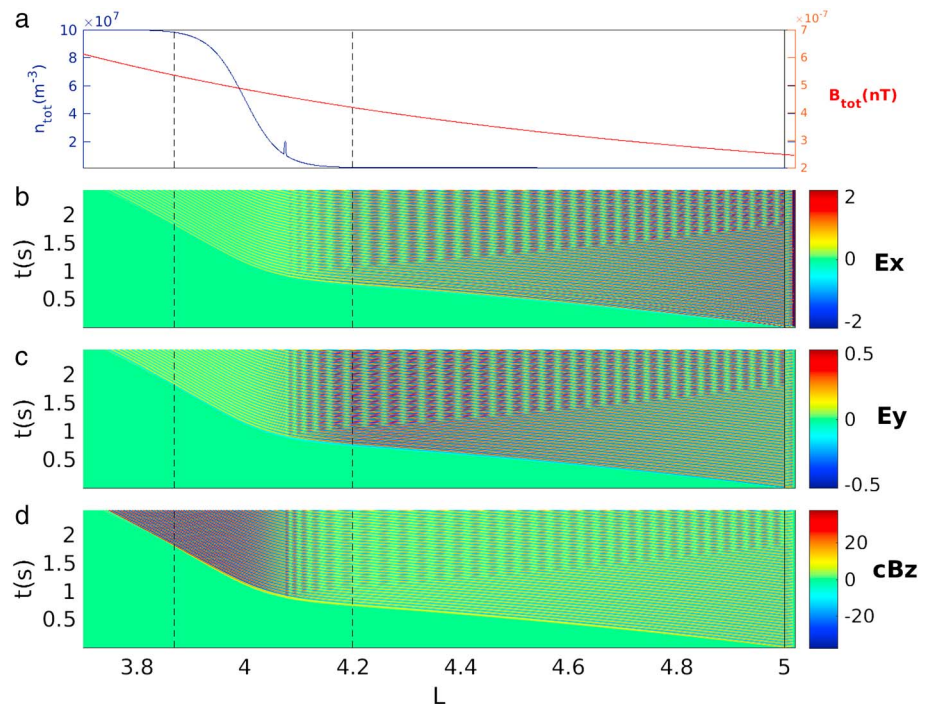


**Figure 6.** MS wave propagation simulation with a single fine-scale density structure in the plasmopause boundary layer in similar format to Figure 4. The source frequency  $(\frac{\omega}{\Omega_{cp}})_s = 5$ .

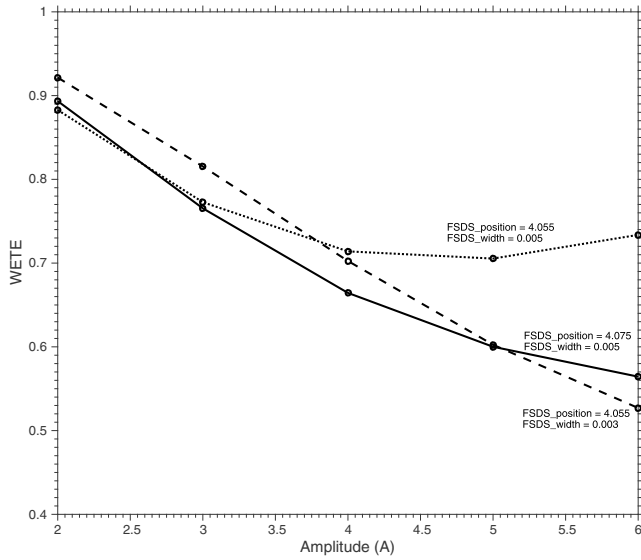


**Figure 7.** The effect of the amplitude of a single fine-scale density structure on WETE for three different combinations of the position and width of the single fine-scale density structure: 4.075  $R_E$  and 0.005  $R_E$  (solid line), 4.055  $R_E$  and 0.003  $R_E$  (dashed line), and 4.055  $R_E$  and 0.005  $R_E$  (dotted line).

to  $|\tilde{E}_y|$  component (Figure 4b), because according to cold dispersion relation,  $\tilde{E}_x/\tilde{E}_y \sim \omega/i\Omega_{cp}$  (derivation of this relation is shown in Appendix A), independent of the value of plasma density. (3)  $|\tilde{B}_z|$  is enhanced inside the plasmopause, compared with the value outside of plasmopause (Figure 4d) because  $\tilde{B}_z = \frac{\eta}{c}\tilde{E}_y \sim \eta^{1/2}$ . (4) The inward propagating wave slows down when passing through the plasmopause where the density increases dramatically, because of the decrease in Alfvén velocity and thus in phase velocity of MS wave.

Next, we fix the plasmopause center location  $L_{pp}$  and examine the effect of its width  $\Delta L_{pp}$  on the WETE. Figure 5 shows the WETE versus  $\Delta L_{pp}$  for three different wave frequencies ( $(\frac{\omega}{\Omega_{cp}})_s = 5, 10, \text{ and } 20$ ). For each wave frequency we mark a critical plasmopause width  $\Delta L_c$  ( $\Delta L_{c5}$ ,  $\Delta L_{c10}$ , and  $\Delta L_{c20}$  in Figure 5) below which the WETE drops dramatically. When the plasmopause width is larger than  $\Delta L_c$ , WETE is almost constant near 1.

When plasmopause width is less than  $\Delta L_c$ , significant portion of wave power is reflected, which cannot be captured by ray tracing method.  $\Delta L_c$  of higher-frequency wave is smaller, because of higher wave number  $k$ . Note that the phase velocity of MS wave nearly equals to Alfvén velocity. The product of wave number  $k_{\text{wave}}$  and critical plasmopause width  $\Delta L$  at  $\Delta L_c$  is about  $6\pi$  (shown in Figure 5). When the plasmopause width is beyond  $\Delta L_c$ , the WETE is larger than 0.8, meaning that the MS wave can propagate through plasmopause without power attenuation beyond  $\Delta L_c$  and ray tracing method works well in this regime.

### 3.3. MS Wave Propagation With a Plasmopause Accompanied With Density Irregularities

The plasmopause can influence the MS wave propagation when plasmopause width is smaller than  $\Delta L_c$  as shown in section 3.2. The value of  $\Delta L_c$ , however, is much smaller than a typical plasmopause width, which is 0.1–1  $R_E$  (Carpenter & Anderson, 1992). Such realistic plasmopause width will unlikely lead to substantial reflection (i.e., a low value of WETE). Nonetheless, the plasmopause is usually not a smooth boundary layer and, in fact, it often accompanies with many fine-scale density structures (e.g., Carpenter & Anderson, 1992 and our Figure 1).

For simulating the effect of those fine structures, we construct a density profile including a typical plasmopause and a fine density peak structure. The plasmopause density profile is set by equation (10). The plasmopause center location  $L_{pp}$  and plasmopause width  $\Delta L_{pp}$  are set to 4 and 0.3, respectively. A fine-scale density structure profile is given by a sinusoidal density variation for simplicity. So the total density can be expressed as

$$n = n_0 \begin{cases} 1 + (A - 1) \sin\left(\pi \frac{L - \frac{2L_s - \Delta L_s}{2}}{\Delta L_s}\right) & L_s - \frac{\Delta L_s}{2} \leq L \leq L_s + \frac{\Delta L_s}{2} \\ = n_0 & \text{otherwise} \end{cases} \quad (16)$$

where  $n_0$  represents the smooth plasmopause density profile and  $A$  is the amplitude of the fine-scale density structure measuring the ratio of the peak density value of the fine-scale structure to the density without the structure.  $L_s$  and  $\Delta L_s$  are the center location and the width of the fine-scale density structure, respectively. We run a simulation for the same wave source location and frequency as those shown in Figure 2. The fine-scale density structure locates at  $L_s = 4.075$ , with its width  $\Delta L_s = 0.005$  and amplitude  $A = 2$ . Figure 6 shows, in a similar format to Figure 4, the simulation result considering fine-scale density structure. We find that the reflection occurs at the location of the fine-scale density structure. A standing wave forms between the fine-scale density structure location and the source location. The WETE decreases from 0.95 to 0.89 due to the single fine-scale density irregularity. We run a case of density valley with same conditions except the amplitude  $A = 0.3$ , which also leads to the WETE decreases (from 0.95 to 0.89; not shown).

Then, we vary the  $A$ ,  $L_s$ , and  $\Delta L_s$  to examine the effect of the amplitude, position, and width of the fine-scale density structures on the WETE for a fixed plasmopause. We run three combinations: (1)  $L_s = 4.055$  and  $\Delta L_s = 0.005$ , (2)  $L_s = 4.075$  and  $\Delta L_s = 0.005$ , and (3)  $L_s = 4.055$  and  $\Delta L_s = 0.003$ . Figure 7 shows the calculated

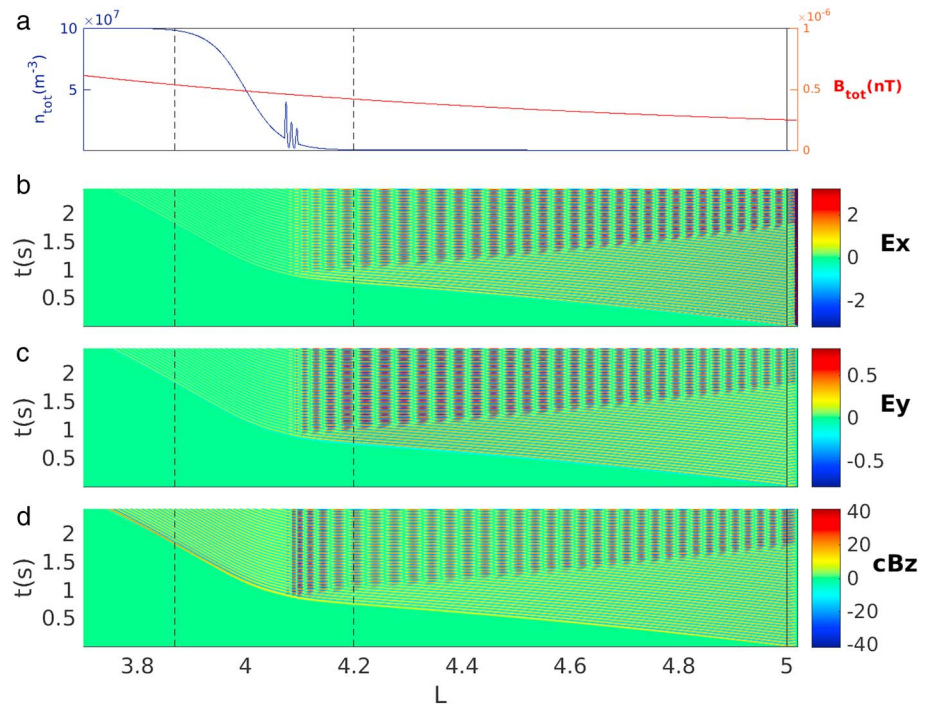


**Figure 8.** MS wave propagation simulation with five fine-scale density structures (three peaks and two valleys) in the plasmapause boundary layer in similar format to Figure 4. The source frequency  $(\frac{\omega}{\Omega_{cp}})_s = 5$ .

WETE versus  $A$  for the three different combinations of  $L_s$  and  $\Delta L_s$ . In general, the WETE decreases with increasing amplitude  $A$  (the solid and dashed lines in Figure 7). When the fine-scale density structure location is closer to the plasmapause center location (the dotted line in Figure 7), the WETE becomes less sensitive to the amplitude with the WETE varying between 0.7 and 0.9. We also examine the fine-scale density structures at the higher-density region of the plasmapause layer (not shown) and find that the fine-scale density structures, either peak ( $n/n_0 > 1$ ) or valley ( $n/n_0 < 1$ ), hardly affect the WETE. Comparing the solid and dotted lines in Figure 7, the fine-scale density structure in the lower-density region is more effective to prevent the radial propagation of the MS wave (reducing the value of WETE). Comparing the dashed and dotted lines in Figure 7, one can find that narrower fine-scale density structures tend to reduce WETE.

Typically, a plasmapause boundary layer accompanies many fine-scale density structures at its outer edge. To examine the effect of such plasmapause, we rerun the simulation shown in Figure 6 by adding density structures of three fine-scale peaks and two fine-scale valleys between three fine-scale peaks (shown in Figure 8a). Each of the five fine density structures is constructed according to equation (16). The center locations of three fine-scale peaks (two fine-scale valleys) are  $L = 4.075, 4.085, 4.095$  (4.08 and 4.09), respectively, and their widths and amplitudes are 0.005 (0.005) and 4 (0.3), respectively. The WETE for this run is 0.154, meaning that the wave is essentially reflected by such plasmapause with density irregularities. The presence of multiple fine-scale structures reduces the WETE value more effectively than a single fine-scale structure (in Figure 6).

#### 4. Conclusions and Discussion

One-dimensional magnetosonic wave propagation in the Earth's dipole field is simulated by finite difference time domain method. Three different density profiles (no plasmapause, with a plasmapause, and fine-scale density structures inside the plasmapause layer) are considered to examine the role of plasmapause on radially propagating MS waves. Our principal conclusions are as follows:

1. Without plasmapause, radially inward propagating MS waves can propagate down to ionosphere altitude if no damping mechanism is considered.
2. WKB approximation is generally valid for a typical plasmapause of width  $0.1 - 1 R_E$ , which only overestimates transmitted wave energy only by  $< \sim 10\%$ .

3. The multiple fine-scale density structures especially near the outer edge of the plasmopause can effectively block the MS wave propagation, and therefore, such plasmopause can serve as a terminating boundary for MS waves.

A recent study (Li et al., 2017) reports that zipper-like MS emissions, which appear as two bands of periodic rising tone MS waves mostly observed at the outside of the plasmopause. The two bands do not appear at the same time. Instead, they seem to alternate in space and resemble the two sides of a “zipper.” The periodic structure observation of MS wave outside the plasmopause is consistent with our simulation results, that is, the structure of standing waves due to reflection by the plasmopause with density irregularities (in Figures 6 and 8). Our simulation of standing waves shows that the spacing between two consecutive power peaks is about  $\lambda/2$ , where  $\lambda$  is the wavelength. We check the event shown in Figure 2 of Li et al. (2017) and find that the separation between the neighboring elements at center frequency of 100 Hz is about  $\frac{3}{2}\lambda$ , comparable to the wavelength scale. Slightly higher separation in the observation may be due to that the spacecraft trajectory was not along wave propagation direction, which leads to longer apparent wavelength. Furthermore, the spacing of observed elements tends to decrease with increasing  $L$ , which is due to the decrease of wavelength. This is also captured in our simulation (see Figures 6 and 8).

Our one-dimensional FDTD model allows us to understand the role of the plasmopause and the density irregularities on radial propagation. The cutoff of MS waves near the plasmopause region (as shown in Figure 1) can be interpreted as the effect of fine-scale density irregularity at the outer edge of the plasmopause layer. We expect that this is also true, in general, including MS waves which are incident at the plasmopause with a finite azimuthal component of wave number. The observed MS waves mainly propagate near the geomagnetic equatorial plane within  $\pm 10^\circ$ . The azimuthal variations of density and background magnetic field are also important for MS wave propagation as demonstrated in previous ray tracing studies (e.g., Chen & Thorne, 2012). In addition, MS wave growth and damping rates depend on background plasma density (e.g., Figure 6 of Chen et al., 2010). Such dependence is also confirmed by the recent Van Allen Probes observation (Yuan et al., 2017). As noted by Boardsen et al. (1992), the differences in raypath and wave normal angle variation between exactly perpendicular propagation and nearly perpendicular propagation are smaller for lower-frequency portion. The latitudinal variation amplitude at nearly perpendicular propagation increases for higher-frequency portion. A 2-D or 3-D FDTD model with consideration of wave growth and damping rates is necessary to fully characterize the nearly perpendicular MS propagation and distribution in the Earth’s magnetosphere.

### Appendix A: Relation for $\tilde{E}_x/\tilde{E}_y$

For MS waves, the wave frequency  $\omega$  satisfies  $\Omega_{cp} < \omega < \omega_{LHR} \ll |\Omega_{ce}|$ , where  $\omega_{LHR}$  is the lower hybrid resonance frequency. The quantities  $R$ ,  $L$ ,  $S$ , and  $D$  in Stix notations can be written as

$$R = 1 + \frac{c^2}{v_{Ap}^2} \frac{1}{m+1} \quad (A1)$$

$$L = 1 - \frac{c^2}{v_{Ap}^2} \frac{1}{m-1} \quad (A2)$$

$$S = \frac{c^2}{v_{Ap}^2} \left( \frac{1}{m_{LHR}^2} - \frac{1}{m^2 - 1} \right) \quad (A3)$$

and

$$D = \frac{c^2}{v_{Ap}^2} \frac{m}{m^2 - 1} \quad (A4)$$

where  $v_{Ap} = \frac{B}{(n_p m_p \mu_0)^{1/2}}$  is proton Alfvénic speed,  $m$  denotes the ratio  $\frac{\omega}{\Omega_{cp}}$ , and  $m_{LHR} = \frac{\omega_{LHR}}{\Omega_{cp}} \approx 42.85$ . The relations  $\frac{\omega_{pp}^2}{\Omega_{cp}^2} = \frac{c^2}{v_{Ap}^2}$ ,  $\frac{\omega_{pe}^2}{|\Omega_{ce}|} = \frac{\omega_{pp}^2}{\Omega_{cp}^2}$  and  $\omega \ll |\Omega_{ce}|$  are used. In Earth’s magnetosphere,  $\frac{c^2}{v_{Ap}^2} \sim 10^4$  and  $m \sim 10^0$ , so  $R$  and  $L$  can be simplified as

$$R = \frac{c^2}{v_{Ap}^2} \frac{1}{m+1} \quad (A5)$$

and

$$L = -\frac{c^2}{v_{Ap}^2} \frac{1}{m-1} \quad (\text{A6})$$

According to the linear dispersion relation of perpendicular direction (Stix, 1992)

$$\frac{\tilde{E}_x}{\tilde{E}_y} = \frac{RL}{S} - S \quad (\text{A7})$$

which can be simplified using the relations above as

$$\frac{\tilde{E}_x}{\tilde{E}_y} = \frac{i}{m} \left( \frac{m_{LHR}^2(m^2-1)}{m^2-1-m_{LHR}^2} + \frac{m^2-1-m_{LHR}^2}{m_{LHR}^2} \right) \quad (\text{A8})$$

For  $m^2 \ll m_{LHR}^2$  (e.g.,  $m = 5$  for the case shown in Figure 4), the expression A8 can be simplified further as

$$\frac{\tilde{E}_x}{\tilde{E}_y} = \frac{m}{i} = \frac{\omega}{i\Omega_{cp}} \quad (\text{A9})$$

#### Acknowledgments

We acknowledge NSF grants 1405041 and 1705079 through the Geospace Environment Modeling program and the AFOSR grant FA9550-16-1-0344. We acknowledge the Van Allen Probes data from the EMFISIS instrument obtained from <https://emfisis.physics.uiowa.edu/data/index> and the EFW instrument data obtained from <http://www.space.umn.edu/missions/rbspewhome-university-of-minnesota/>.

#### References

- Balikhin, M. A., Shprits, Y. Y., Walker, S. N., Chen, L., Cornilleau-Wehrlin, N., Dandouras, I., ... Weiss, B. (2015). Observations of discrete harmonics emerging from equatorial noise. *Nature Communications*, 6, 7703. <https://doi.org/10.1038/ncomms8703>
- Boardsen, S. A., Gallagher, D. L., Gurnett, D. A., Peterson, W. K., & Green, J. L. (1992). Funnel-shaped, low-frequency equatorial waves. *Journal of Geophysical Research*, 97(A10), 14,967–14,976. <https://doi.org/10.1029/92JA00827>
- Boardsen, S. A., Hospodarsky, G. B., Kletzing, C. A., Engebretson, M. J., Pfaff, R. F., Wygant, J. R., ... De Pascuale, S. (2016). Survey of the frequency dependent latitudinal distribution of the fast magnetosonic wave mode from Van Allen Probes electric and magnetic field instrument and integrated science waveform receiver plasma wave analysis. *Journal of Geophysical Research: Space Physics*, 121, 2902–2921. <https://doi.org/10.1002/2015JA021844>
- Boardsen, S. A., Hospodarsky, G. B., Kletzing, C. A., Pfaff, R. F., Kurth, W. S., Wygant, J. R., & MacDonald, E. A. (2014). Van Allen Probe observations of periodic rising frequencies of the fast magnetosonic mode. *Geophysical Research Letters*, 41, 8161–8168. <https://doi.org/10.1002/2014GL020200>
- Bortnik, J., Chen, L., Li, W., Thorne, R. M., & Horne, R. B. (2011). Modeling the evolution of chorus waves into plasmaspheric hiss. *Journal of Geophysical Research*, 116, A08221. <https://doi.org/10.1029/2011JA016499>
- Carpenter, D. L., & Anderson, R. R. (1992). An ISEE/Whistler model of equatorial electron density in the magnetosphere. *Journal of Geophysical Research*, 97(A2), 1097–1108.
- Chen, L. (2015). Wave normal angle and frequency characteristics of magnetosonic wave linear instability. *Geophysical Research Letters*, 42, 4709–4715. <https://doi.org/10.1002/2015GL064237>
- Chen, L., & Thorne, R. M. (2012). Perpendicular propagation of magnetosonic waves. *Geophysical Research Letters*, 39, L14102. <https://doi.org/10.1029/2012GL052485>
- Chen, L., Thorne, R. M., Jordanova, V. K., Wang, C., Gkioulidou, M., Lyons, L., & Horne, R. B. (2010). Global simulation of EMIC wave excitation during the 21 April 2001 storm from coupled RCM-RAM-HOTRAY modeling. *Journal of Geophysical Research*, 115, A07209. <https://doi.org/10.1029/2009JA015075>
- Fu, H. S., Cao, J. B., Zhima, Z., Khotyaintsev, Y. V., Angelopoulos, V., Santolík, O., ... Huang, S. Y. (2014). First observation of rising-tone magnetosonic waves. *Geophysical Research Letters*, 41, 7419–7426. <https://doi.org/10.1002/2014GL061867>
- Gul'elmi, A., Klaine, B., & Potapov, A. (1975). Excitation of magnetosonic waves with discrete spectrum in the equatorial vicinity of the plasmapause. *Planetary and Space Science*, 23(2), 279–286. [https://doi.org/10.1016/0032-0633\(75\)90133-6](https://doi.org/10.1016/0032-0633(75)90133-6)
- Gurnett, D. A. (1976). Plasma wave interactions with energetic ions near the magnetic equator. *Journal of Geophysical Research*, 81, 2765–2770. <https://doi.org/10.1029/JA081i016p02765>
- Hrbáčková, Z., Santolík, F., Němec, Macúšová, E., & Cornilleau-Wehrlin, N. (2015). Systematic analysis of occurrence of equatorial noise emissions using 10 years of data from the cluster mission. *Journal of Geophysical Research: Space Physics*, 120, 1007–1021. <https://doi.org/10.1002/2014JA020268>
- Kletzing, C. A., Kurth, W. S., Acuna, M., MacDowall, R. J., Torbert, R. B., Averkamp, T., ... Tyler, J. (2013). The Electric and Magnetic Field Instrument Suite and Integrated Science (EMFISIS) on RBSP. *Space Science Reviews*, 179(1), 127–181. <https://doi.org/10.1007/s11214-013-9993-6>
- Laakso, H., Junginger, H., Schmidt, R., Roux, A., & de Villedary, C. (1990). Magnetosonic waves above  $f_c(H^+)$  at geostationary orbit: GEOS 2 results. *Journal of Geophysical Research*, 95, 10,609–10,621. <https://doi.org/10.1029/JA095iA07p10609>
- Li, J., Bortnik, J., Li, W., Ma, Q., Thorne, R. M., Kletzing, C. A., ... Russell, C. T. (2017). "Zipper-like" periodic magnetosonic waves: Van Allen Probes, THEMIS, and magnetospheric multiscale observations. *Journal of Geophysical Research: Space Physics*, 122, 1600–1610. <https://doi.org/10.1002/2016JA023536>
- Mauk, B. H., Fox, N. J., Kanekal, S. G., Kessel, R. L., Sibeck, D. G., & Ukhorskiy, A. (2013). Science objectives and rationale for the radiation belt storm probes mission. *Space Science Reviews*, 179(1), 3–27. <https://doi.org/10.1007/s11214-012-9908-y>
- Němec, F., Santolík, O., Gereová, K., Macúšová, E., de Conchy, Y., & Cornilleau-Wehrlin, N. (2005). Initial results of a survey of equatorial noise emissions observed by the Cluster spacecraft. *Planetary and Space Science*, 53, 291–298. <https://doi.org/10.1016/j.pss.2004.09.055>
- Olsen, R. C., Shawhan, S. D., Gallagher, D. L., Chappell, C. R., & Green, J. L. (1987). Plasma observations at the Earth's magnetic equator. *Journal of Geophysical Research*, 92, 2385–2407. <https://doi.org/10.1029/JA092iA03p02385>
- Perraut, S., Roux, A., Robert, P., Gendrin, R., Sauvaud, J.-A., Bosqued, J.-M., ... Korth, A. (1982). A systematic study of ULF waves above  $F_{H^+}$  from GEOS 1 and 2 measurements and their relationships with proton ring distributions. *Journal of Geophysical Research*, 87, 6219–6236. <https://doi.org/10.1029/JA087iA08p06219>

- Russell, C. T., Holzer, R. E., & Smith, E. J. (1970). OGO 3 observations of ELF noise in the magnetosphere: 2. The nature of the equatorial noise. *Journal of Geophysical Research*, *75*, 755–768. <https://doi.org/10.1029/JA075i004p00755>
- Santolik, O., Nemeč, F., Gereová, K., Macúšová, E., Conchy, Y., & Cornilleau-Wehrin, N. (2004). Systematic analysis of equatorial noise below the lower hybrid frequency. *Annales Geophysicae*, *22*, 2587–2595. <https://doi.org/10.5194/angeo-22-2587-2004>
- Santolik, O., Parrot, M., & Nemeč, F. (2016). Propagation of equatorial noise to low altitudes: Decoupling from the magnetosonic mode. *Geophysical Research Letters*, *43*, 6694–6704. <https://doi.org/10.1002/2016GL069582>
- Santolik, O., Pickett, J. S., Gurnett, D. A., Maksimovic, M., & Cornilleau-Wehrin, N. (2002). Spatiotemporal variability and propagation of equatorial noise observed by Cluster. *Journal of Geophysical Research*, *107*, 1495. <https://doi.org/10.1029/2001JA009159>
- Shi, L.-J., Yang, L.-X., Cai, Z.-C., & Ding, J.-N. (2015). An FDTD absorbing boundary condition for anisotropic media based on NPML. *Waves in Random and Complex Media*, *25*(2), 293–305. <https://doi.org/10.1080/17455030.2015.1020907>
- Stix (1992). *Waves in plasmas*. College Park, MD: American Institute of Physics.
- Sun, J., Gao, X., Chen, L., Lu, Q., Tao, X., & Wang, S. (2016). A parametric study for the generation of ion Bernstein modes from a discrete spectrum to a continuous one in the inner magnetosphere. I. Linear theory. *Physics of Plasmas*, *23*(2), 022901. <https://doi.org/10.1063/1.4941283>
- Sun, J., Gao, X., Lu, Q., Chen, L., Tao, X., & Wang, S. (2016). A parametric study for the generation of ion Bernstein modes from a discrete spectrum to a continuous one in the inner magnetosphere. II. Particle-in-cell simulations. *Physics of Plasmas*, *23*(2), 022902. <https://doi.org/10.1063/1.4941284>
- Wygant, J. R., Bonnell, J. W., Goetz, K., Ergun, R. E., Mozer, F. S., Bale, S. D., ... Tao, J. B. (2013). The electric field and waves instruments on the radiation belt storm probes mission. *Space Science Reviews*, *179*(1), 183–220. <https://doi.org/10.1007/s11214-013-0013-7>
- Xiao, F., Zhou, Q., He, Z., & Tang, L. (2012). Three-dimensional ray tracing of fast magnetosonic waves. *Journal of Geophysical Research*, *117*, A06208. <https://doi.org/10.1029/2012JA017589>
- Xie, Y.-T., & Yang, L.-X. (2011). Bandgap characteristics of 2D plasma photonic crystal with oblique incidence: TM case. *Chinese Physics B*, *20*(6), 060201.
- Yang, L., Xie, Y., & Yu, P. (2011). Study of bandgap characteristics of 2D magnetoplasma photonic crystal by using M-FDTD method. *Microwave and Optical Technology Letters*, *53*(8), 1778–1784. <https://doi.org/10.1002/mop.26143>
- Yuan, Z., Yu, X., Huang, S., Wang, D., & Funsten, H. O. (2017). In situ observations of magnetosonic waves modulated by background plasma density. *Geophysical Research Letters*, *44*, 7628–7633. <https://doi.org/10.1002/2017GL074681>
- Zhima, Z., Chen, L., Fu, H., Cao, J., Horne, R. B., & Reeves, G. (2015). Observations of discrete magnetosonic waves off the magnetic equator. *Geophysical Research Letters*, *42*, 9694–9701. <https://doi.org/10.1002/2015GL066255>